

TURBULENCE MEASUREMENTS OF A SIMPLIFIED UNDERHOOD AUTOMOTIVE FLOW

Keith Paschal, Chungsheng Yao, and Scott Bartram
NASA LaRC
Hampton, Virginia

David Shack
Automated Analysis Corporation
Ann Arbor, Michigan

George Shih
FORD Motor Company
Dearborn, Michigan

ABSTRACT

Flowfield measurements were obtained of the turbulence characteristics of a simplified automotive flow. Particle Image Velocimetry (PIV) data was used to compute mean and turbulence quantities of the underhood flow in a simplified automotive model (the Boxcar). Laser Velocimetry (LV) was used to estimate inlet and exit mass flow rates of the engine compartment. Previously this geometry was used as a validation tool against which commercially available CFD codes were evaluated. The goal of the present study was to generate a reference data set for validation purposes. The mean flow field was computed, the underhood turbulent shear regions were characterized, and inlet and exit mass flow rates were estimated. A cross-correlation technique was used to interrogate the film-based PIV images that were acquired along the Boxcar centerline. The technique provided a resolution of 1 mm in all three spatial directions. Mean flow and second-order moments were computed and have shown the existence of a potential core between the Boxcar air-inlet and engine block. On either side of this potential core shear regions developed. Correlations have been computed in the upper shear layer to determine relevant turbulent length scales. Also, estimates of eddy viscosity in this shear region have been computed. Mean and instantaneous velocity fields behind the engine block have shown the presence of a fairly stable counter-clockwise vortex.

NOMENCLATURE

C_{uu}, C_{vv}	spatial velocity autocorrelations
ℓ_{mv}	length of square PIV interrogation area
ℓ	integral length scale
R_ℓ	turbulent Reynolds number
U, V	mean velocity components
u, v	instantaneous velocity components
u', v'	fluctuating velocity components
u_{rms}	characteristic rms velocity
$\langle u'v' \rangle$	Reynolds stress
x, y, z	streamwise, wall-normal, and spanwise coordinates
Δ	displacement of double-exposed particle images
κ	half angle of LV beam intersection
ν	kinematic viscosity
ν_t	eddy viscosity
∞	denotes freestream condition
$\langle \rangle$	denotes ensemble average

INTRODUCTION

The automotive industry is increasing the use of Computer Aided Engineering (CAE) methods to reduce design cycle time and the dependency on testing. One area where computational techniques can play a significant role is the analysis of airflow in a car's underhood compartment. Underhood air flows have a major influence on engine cooling, as well as on the underhood temperature distribution. This temperature distribution is critical for designers, as it affects the performance and reliability of the many auxiliary components found under the hood. While knowledge of the underhood flow patterns, and ultimately of the cooling performance and temperature distribution, is vital to the design process, gaining this knowledge has traditionally posed some difficulties. The geometry of the underhood compartment and the placement and shape of the various components that it contains undergoes nearly continuous revision during the design cycle. By the time the airflow in a given configuration has been investigated experimentally, the configuration will likely be obsolete.

Computational fluid dynamics (CFD) can alleviate this difficulty by providing a more expedient return of airflow results to the designers. Without the need to construct physical models and schedule precious wind tunnel time, CFD can be used to quickly react to design changes. In addition to evaluating interim designs, CFD can also be used to evaluate the viability of proposed designs before they are committed to hardware (Davis, et. al., 1993).

Before effectively employing a CFD code, its limitations must be well understood and its performance must be thoroughly characterized. An experimental program is required to provide empirical data for use in benchmarking the code. The test program should be designed to evaluate the code's ability to model the flow physics encountered, as well as to calibrate the analytical results so that they can be used to guide the design process (Marvin, 1988). The work described in this paper is part of such a program. In this case, a simplified automobile geometry is used to generate reference velocity and flow data.

The rationale for this simplified geometry is detailed in Shack, et. al. (1995). Briefly, this geometry was chosen so that analysis and measurement could be done more simply than in a production geometry. The configuration is much simpler to mesh than typical production geometry, so preprocessing takes less time, allowing more codes to be investigated. It is also much easier to make velocity measurements in the simplified geometry since it incorporates transparent planar surfaces and a relatively empty engine compartment.

These features allow the use of laser-based diagnostic techniques such as PIV and LV, which are difficult to use in an actual engine compartment. Despite the relatively simple geometry, the flows encountered in this configuration are complex and three dimensional (Shack, et. al., 1995), and present a challenge for both measurement and analysis. Future work will involve actual production configurations to complete the evaluation of the selected CFD codes.

EXPERIMENTAL DESCRIPTION

Experimental Setup

PIV and LV measurements were made in a 38x38 mm closed-return low-speed wind tunnel. The geometry of the Boxcar is shown in Fig. 1. The Boxcar was 33.9 mm long, 12.7 mm wide, and stood 7.4 mm high. The engine compartment was 8.5 mm long, 12.7 mm wide and 5.3 mm high. The aft end of the model was constructed of aluminum while the engine compartment was made of glass for optical access. Note that the engine block was offset towards the passenger side of the Boxcar. To remove effects from the tunnel floor boundary layer the model was mounted on a splitter plate one Boxcar length downstream of the leading edge. The starting point of the floor boundary layer was fixed by the splitter plate as well.

The Boxcar was a scaled replica of the model described in Shack, et. al., 1995. Like the previous model, this model was instrumented for pressure measurements. However, none of our pressure measurements will be presented as good agreement was seen between both sets of data. Shack, et. al., 1995, documented pressure distributions, mean flow (at four underhood spanwise planar locations), and attested to the highly complex 3-D flow field. This paper will be mainly concerned with a detailed look at the underhood flow along the centerline plane. Shack, et. al., 1995, provides more insight into the geometry, design and testing philosophy behind the Boxcar model.

PIV measurements were made along the centerline (x-y plane) of the Boxcar engine compartment with freestream velocity held at 40 m/s. Single component LV measurements were made in the y-z plane of the air inlet, and in the four x-z exit planes located on the floor of the engine compartment. There were two exit planes on each side of the model, one in front of the wheel block and one behind. Mass flow rates were estimated for U_∞ of 20 m/s and 32 m/s.

PIV data was used to determine mean and fluctuating properties of this flow. PIV is a global technique that measures instantaneous velocity vectors in a plane.

A planar light sheet is used to illuminate micron sized particles seeded in the flow. Particle double-exposed photographs are taken, and instantaneous velocity is determined from particle displacements. Figure 2 shows the mean flow field in front of the Boxcar, underhood in front of the engine block, and underhood aft of the engine block. Every other velocity vector was plotted in both directions to simplify viewing of the velocity field. All the PIV data was taken in this x-y plane along the centerline of the Boxcar. More information on the PIV technique will be presented in the following section.

A TSI six jet atomizer was used to generate high concentrations of seed particles required for both optical techniques. The resulting mineral oil particles had an average diameter of less than $1\text{ }\mu\text{m}$ according to TSI specifications. The largest particles were estimated to track turbulent eddies within 5% of the velocity difference across the internal shear layer (Adrian, 1991).

PIV System

In this section the PIV system will be briefly described. A more detailed explanation of the optical setup and operation is given in Yao and Paschal (1994). Reviews by Adrian (1991) and Buchave (1992) provide general information on PIV and its status. This section will cover our lasers and optics, camera and image shifting device, and interrogation software and hardware.

Two Nd:Yag lasers illuminated the test plane with approximately 550 mJ energy output per pulse at 532 nm wavelength. The optical table layout of the Yag lasers and optics is shown in figure 3. The second Yag was oriented 22.5° from the first so that its beam could be combined at the polarizer while maintaining right angle mirror reflections. A half-wave plate was used to rotate the polarization of the second beam 90° relative to the first beam. Cross-polarization between the two beams was required for the image shifting technique that removed flow direction ambiguity. After beam combination at the polarizer a light sheet with adjustable focal length, width, and thickness was formed. For this test the light sheet in the test section was measured 100 mm wide and less than 1 mm thick. The laser pulse separation was $5.000 \pm 0.001\text{ }\mu\text{s}$ and the duration of each pulse was between 5 and 7 ns.

A 4"x5" format camera with a 300 mm focal length processor lens was used to record particle images at 1:1 magnification. The long focal length lens was used to minimize the out-of-plane displacement error and the measurement area covered up to 120x100 mm at 1:1 imaging. A 25 mm square calcite crystal was placed in front of the camera to remove flow direction

ambiguity. The 1.3 mm thick calcite plate removed flow direction ambiguity by shifting the vertically polarized beam downward 0.13 mm. The specifications of the plate followed the design of Landreth and Adrian (1988). The exposure of micron-sized oil particles at an aperture setting of f/11 was satisfactory at maximum laser energy output. The particle images were recorded on TMAX 400 film and measured 20–30 μm in diameter. These images were almost aberration-free and showed negligible geometry distortion.

Double exposed particle images were analyzed on a UNIX workstation. A CID (charge injection device) camera with a resolution of 512x512 pixels and 50 mm enlarger lens sampled images from a small portion (approximately 3.5 mm square) of the PIV photograph. The interrogation camera was calibrated using a grating pattern of 100 lines per inch and the accuracy of the interrogation magnification was within 0.5%. A frame grabber transferred the particle images to the interrogation computer, which incorporated an i860 high-speed floating-point processor to compute image cross-correlations of a sub-region of the sampled frame. The size of the sub-region defined the PIV interrogation area and spatial resolution in the x and y-directions. Spatial resolution in both the x and y-directions was 1 mm for this study.

The resolution in the spanwise direction was fixed for this study. PIV employed a light sheet with a fixed thickness to illuminate particles tracking the flow. An imaging lens was used to record the particle images. This lens integrated over the thickness of the light sheet to produce a 2-D picture of the double-exposed particles. The thickness of the laser sheet is equivalent to the spanwise spatial resolution and was approximately 1 mm for this study.

PIV data were interrogated with a cross correlation technique that shifted the second image with respect to the first image by 18 pixels in the y-direction. This shift corresponded to that imposed by the calcite crystal. Since there was no shift in the x-direction, the displacement of the double exposed images relative to the length of the interrogation area (Δ/ℓ_{mv}) was held < 0.25 as suggested by Keane and Adrian (1990) to reduce velocity bias in regions of large velocity gradients. The cross-correlation was computed on a 128x128 pixel area and took approximately 0.080 seconds. Nyquist sampling criterion required over-sampling of the interrogation area by 50%. More detailed information is given in Yao and Paschal (1994).

A semi-automated post-interrogation code was used to remove erroneous vectors. A 3x3 binomial filter was used to smooth the instantaneous velocity fields

and remove random high-frequency noise. Mean, turbulence statistics, and correlations were then computed.

LV System

A 3 component, commercially available LV system was used to obtain velocity measurements for the mass flow estimates. The system consisted of a 5-watt argon ion laser, a beam-splitter unit, processing electronics, and fiber-optic probes (Fig. 4). The beam-splitter unit was used to separate the laser output into 3 distinct wavelengths, green (514.5 nm), blue (488 nm) and violet (476.5 nm). This unit also split each individual wavelength into two beams, one being shifted 40 MHz to allow determination of flow direction. This system employed two fiber-optic heads, the green and blue beams were passed to the first probe and the violet beams were passed to the second probe. Each probe contained both transmitting and receiving optics. A single channel (one probe) was used for our application as 1-D measurements were required for estimation of the mass flow rates.

Output from the probe was received by the Photomultiplier tube, converted to an electrical signal, and passed to the Autocorrelator unit. This unit used a double-clipped, discrete autocorrelation function to extract the Doppler frequency. The advantage of the autocorrelation technique lies in its ability to isolate the correlated Doppler signal from the uncorrelated noise components.

The probe was oriented in the x-z plane as shown in Fig. 5 for the measurement of flow into the engine compartment. One of the two beams was aligned parallel with the model surface along the z-axis to allow accurate measurements only a small distance from the inflow plane. The distance from the parallel beam and the model was less than 500 μm . The outflow velocity measurements were made in a similar manner with the distance between the parallel beam and the outflow plane being approximately 100 μm due to the favorable geometry of the outflow vents.

Note also from Fig. 5 that the measured velocity component was contaminated by the product of the sine of κ and the spanwise velocity. Fortunately the value of κ (2.35°) was small. A similar problem occurred with the outflow velocity measurements. No attempt has been made to correct these measurements with the original CFD computations. Despite this contamination, the inflow mass flow rate was within 10% of the computed outflow mass flow rate for both freestream conditions.

RESULTS AND ANALYSIS

Internal and External Mean Flow

The mean flow field was computed by ensemble averaging 42 instantaneous PIV realizations. Figure 2 is a composite of the mean flow field presenting the mean flow in front of the Boxcar, underhood before the engine block, and underhood aft of the engine block. In this section the 3 regions of the flow will be examined individually. Note the coordinate system origin is located on the lower left front corner of the Boxcar, and that +x is downstream of the model. Grid spacing for all the PIV data is 0.5 mm in both x and y-directions, and freestream velocity is 40 m/s.

Profiles of the U-component of the freestream flow are presented in Fig 6. Every fourth point was labeled in these plots for ease of viewing. In general U is seen to decrease as the flow approaches the inlet plane (y-z plane at x=0) as one would expect. The y-locations of the Boxcar inlet relative to the profiles show a jet-like flow near the model (x=-6.479 mm). On either side of this core flow are seen low-speed lobes which are associated with stagnation streamlines on either side of the inlet opening. For y-values less than 0.0 mm and greater than approximately 35 mm the flow is seen to accelerate under and over the Boxcar.

Profiles of the V-component of the freestream flow are presented in Fig. 7. In the core region of the flow the vertical velocity component is nominally 5 m/s. On the top side of the core flow (y > 23.5 mm) V is positive and the flow is seen to accelerate over the model. Conversely, on the lower side of the core flow V is negative and the flow is seen to accelerate under the Boxcar.

Flow from the freestream can be seen entering the model through the rectangular air inlet with a small positive flow angle in Fig. 8. The potential core is surrounded by counter rotating vortex structures and has accelerated to approximately 40 m/s through the inlet opening. Strong velocity gradients exist between the core and both vortex centers. The resulting shear layers are constrained by the Boxcar geometry. The upper shear layer will be discussed in more detail in later sections. The lower shear layer was not investigated further as the lower vortex structure was not well resolved. Note that the core velocity of 40 m/s was roughly equivalent to the freestream velocity.

The mean flow field underhood and aft of the engine block is presented in Fig. 9. A single low-speed vortex is shown to exist. The change in velocity magnitude between this flow region and the previous underhood flow region is apparent from the respective

reference velocity vector magnitudes. Figure 2 clearly depicts the differences in the 3 flow regions associated with the Boxcar and demonstrates the dynamic range of the PIV instrument.

Mass Flow Estimates

Inlet and exit LV velocity contours are shown in Figs 10 and 11 for U_∞ of 20 m/s and 32 m/s respectively. For both cases the inflow rate was within 10% of the mass flow rate out of the Boxcar. The flow patterns for both cases are virtually identical, the only difference being velocity magnitudes. The maximum inflow velocities measured were 13 m/s ($U_\infty=20$ m/s) and 20 m/s ($U_\infty=32$ m/s). These were fairly constant values measured along the z-axis at $y = 16.5$ mm (see Fig. 6 for geometry). A simple freestream scaling argument yields the following:

$$\frac{U_{max}}{U_\infty} \sim 0.63$$

This scaling argument also applies to the PIV freestream data previously shown in Fig. 6.

The outflow contours seen in Figs 10 and 11 are very complex with limited flow reversal occurring in the outflow planes. Outflow planes in front of the engine block saw velocities ranging from -20 m/s (exiting the Boxcar) to $+3$ m/s (entering the Boxcar). Outflow planes aft of the engine block saw velocities ranging from -30 m/s to $+1$ m/s. Also, the outflow planes on the driver and passenger sides of the Boxcar aft of the engine block were fairly symmetrical. More detailed flow field measurements inside the model would be required to satisfactorily explain these exit flow patterns.

Fluctuating Nature of Underhood Flow

PIV measures the instantaneous (u,v) velocity field as a $f(x,y)$ at random moments in time. Mean flow is computed by ensemble averaging the instantaneous realizations. The fluctuating instantaneous (u',v') velocity fields are computed by subtracting the mean from each individual instantaneous (u,v) realization. In an attempt to document the fluctuating and unsteady nature of the underhood flow, five fluctuating velocity fields are presented in (Fig. 12–16). Note that the instantaneous (u,v) fields were smoothed using a 3×3 convolution to remove high frequency noise before the mean was computed. The vector validation rate was over 95% for all 42 realizations of the flow field.

The u',v' field in Fig. 12 is characterized by a fairly quiet potential core surrounded by an upper and

lower shear region. The lower shear region is less vigorous than the upper shear for this particular realization. The reference velocity vector is approximately 75% of the maximum potential core velocity.

An extremely active lower shear region is seen in Fig. 13. The lower shear cuts through the potential core vertically at $x=15-20$ mm and forms a vortex structure which interacts with the upper shear. A secondary vortex appears to have been shed at approximately $x,y=(10\text{mm}, 25\text{mm})$. The lower shear fluctuating velocities are on the order of the potential core mean.

The u',v' field in Fig. 14 is similar to the previous field in that the lower and upper shear regions interact to form a vortex structure near the tip of the triangular potential core. The fluctuating magnitudes are considerably lower than shown in the previous case. The spawned secondary eddy is also missing.

Figures 15 and 16 are more typical of the majority of the realizations with a visible potential core surrounded by active upper and lower shear layers. Figure 16 is distinctive in that a counter-rotating vortex pair exists in the upper shear layer. Although the unsteady nature of the flow is difficult to observe from the fluctuating plots, the instantaneous (u,v) plots show the potential core flow angle oscillating between the horizontal and a slight angle from this reference. Note the mean flow (Fig. 8) shows a slight positive flow angle on average.

Turbulence Statistics and Correlations

Two point correlations were computed at a single point in the upper shear layer in order to obtain scale information. The coordinate $x,y=(20.5\text{mm}, 25.5\text{mm})$ was chosen as it lies in the middle of the upper shear along a steep velocity gradient (see Fig. 8). $\langle C_{uu} \rangle$ and $\langle C_{vv} \rangle$ for this point are presented in Fig. 17 and 18. A total of 42 realizations were available to estimate these correlations. $\langle C_{uu} \rangle$ is shown to be stretched along the propagation line of the shear layer while $\langle C_{vv} \rangle$ has a more symmetrical distribution

Integration of the normalized two-point correlations yielded spatial information about the shear layer. The correlations were integrated along both the x and y-directions to produce a total of 4 integral scales of motion. The values with respect to integration along the x-axis are list below:

$$\begin{aligned}\ell_{uu,x} &= 4.60\text{mm} \\ \ell_{vv,x} &= 3.45\text{mm}\end{aligned}$$

The values with respect to y are listed below:

$$\begin{aligned}\ell_{uu,y} &= 2.54\text{mm} \\ \ell_{vv,y} &= 3.05\text{mm}\end{aligned}$$

The length of correlation on average in the x direction is approximately 4 mm, while the correlation length in the y direction is approximately 3 mm. These scales agree qualitatively with those observed from the $\langle C_{uu} \rangle$ and $\langle C_{vv} \rangle$ plots as one would expect.

Based on the previous integral scale results a turbulent Reynolds number may be estimated for this flow. This value represents the importance of turbulent stresses relative to viscous stresses and is defined as follows (Tennekes and Lumley, 1972):

$$R_\ell = \frac{u_{\text{rms}} \ell}{\nu}$$

Defining u_{rms} as the maximum rms value (on the order of 11 m/s) and ℓ as an average of the two characteristic x scales (approximately 4 mm), R_ℓ is approximately 3,000. From this estimate one should expect the turbulent shear layers to dominate the underhood flow in front of the engine block.

The velocity gradients, Reynolds stress, and eddy viscosity have been estimated for the upper shear layer from the 42 instantaneous PIV realizations. The authors previous experience with shear layers indicate that on the order of 200 realizations are required for quantitative agreement between PIV and LV Reynolds stress estimates (Yao and Paschal, 1994; Paschal, et. al., 1994). The Reynolds stress and eddy viscosity should be viewed as estimates of these quantities. Keep in mind that separation of turbulent stresses and effective stresses due to flow unsteadiness are impossible to remove without some type of phase-locked data acquisition scheme.

The velocity gradients are presented in Fig 19 and 20. The contour plot reveals large gradients near the inlet plane and shows the basic structure of the shear. The positive values of shear near the Boxcar hood are due to local erroneous vectors. Figure 20 is a shear profile along $x=20.5$ mm. The largest gradient is shown to exist around $y=25$ mm. Keep in mind the correlations were computed at x,y coordinates of (20.5mm, 25.5mm). As the profile goes through the mean vortex center at x approximately 30 mm (see Fig. 8), the shearing rate stabilizes. On the far side of the mean vortex center the shearing rate again decreases.

Reynolds stress estimates are presented in Fig 21 and 22. For our case the Reynolds stress has been normalized by U_∞ , which is equivalent to U_{max} in

the potential core. The contour plot shows a strong shear layer developing along the edge of the potential core bounded by the Boxcar hood. The y -profile along $x=20.5$ mm shows a peak in the Reynolds stress at approximately $y=25$ mm. The maximum Reynolds stress value in the upper shear is approaching 0.024. Hinze (1987) has measured maximum Reynolds stress values approaching 0.020 in a free jet. The discrepancy between the two values may come from one of many sources. First, more realizations are needed to completely converge the Reynolds stress estimate. Second, this particular underhood shear region is bounded by the Boxcar hood and engine block, which may lead to more vigorous turbulence with higher stresses. Finally, the oscillating potential core flow angle will increase the effective turbulence as well. Regardless, the comparison with Hinze suggests that the estimate of Reynolds stress is a fairly good one.

Estimates of eddy viscosity are presented in Fig 23 and 24. We have defined eddy viscosity as follows:

$$\nu_t = - \frac{\langle \mathbf{u}' \mathbf{v}' \rangle}{\frac{\partial U}{\partial y}}$$

Computed values inside the upper shear are typically less than 0.01 m²/s. Two dominant peaks are seen in the contour pattern ($x=17$ mm and $x=26$ mm). The erroneous values near the engine block and Boxcar hood are in part caused by noisy vectors and possibly the fact that ν_t is ill-defined outside the shear region. Data below $y=22$ mm has been deleted as the definition of eddy viscosity is meaningless in the potential core. Eddy viscosity estimates are presented to show that the PIV instrument has the ability to compute ν_t (given sufficient realizations) and directly compared with CFD results.

Optical Techniques and Internal Flows

The main difficulty with obtaining sufficient quantities of PIV data resulted from seeding problems with the internal flow configuration. High concentrations of mineral oil particles were used to seed the flow. As eluded to earlier, oil based particles were used to satisfy the size and polarization preserving seed constraints imposed by the PIV system. The particles would coat the glass hood assembly and render imaging impossible within 20 minutes testing time. Typically, the camera could be focused and around 20 PIV photographs taken in the allotted time frame. LV measurements through the glass hood assembly were not possible in general. For example, a typical flow exit plane with 200 points (4,000 samples per point) would take over 3 hours to acquire.

While LV is the better tool for the measurement of higher-order turbulent statistics, PIV was the only viable technique with which to obtain statistical information for this particular internal flow. One advantage of LV is that data may be post-processed on-line. PIV required approximately 30–45 minutes of post-processing per realization. The main advantage of PIV lies in its ability to measure the instantaneous field and resolve spatial features of the flow. The application of both techniques to a particular turbulent flow provide accurate turbulent statistics, important spatial information, and a consistency check for the experimental data.

CONCLUSIONS

PIV and LV techniques were used to generate a reference data set for CFD validation of a simplified automotive geometry. PIV was used to provide mean and Reynolds stress information, and general insight into the nature of the flow, from 42 realizations. One important observation was the unsteady behavior of the potential core flow angle underhood in front of the engine block. Length scale information was extracted from velocity correlations, and Re_ℓ was on the order of 3,000 indicating the importance of turbulence relative to viscous effects in the internal shear regions. Eddy viscosity was estimated based on Reynolds stress. Freestream velocity for the PIV measurements was 40 m/s. LV provided 1-D velocity measurements used to compute Boxcar mass inflow and outflow. Mass flow rate was a relatively easy term to compare between codes and provided a good validation parameter. Freestream velocity was 20 and 32 m/s for the LV measurements.

ACKNOWLEDGMENTS

We would like to acknowledge Dr. Carl Meinhart and Dr. Ronald Adrian for support with vector validation techniques, and Greg Jones for the Boxcar pressure distributions.

REFERENCES

- Davis, F.V., Veling, T.R., Caltrider, J.L., and Madhavar, R., 1993, "Impact of Computer Aided Engineering on Ford Motor Company Light Truck Cooling Design and Development Processes," SAE Paper No. 932977.
- Marvin, J.G., 1988, "Accuracy Requirements and Benchmark Experiments for CFD Validation," NASA Technical Memorandum 100087, Ames Research Center, Moffet Field, CA.
- Shack, D.H., Bernal, L.P., and Shih, G.S. 1995, "Experimental Investigation of Underhood Flow in a Simplified Automobile Geometry"
- Yao, C.S., and Paschal K.B., 1994, "PIV Measurements of Airfoil Wake-Flow Turbulence Statistics and Turbulent Structures," AIAA 94-0085, 32nd Aerospace Sciences Meeting and Exhibit, Jan 10-13, 1994, Reno, NV.
- Adrian, R.J., 1991, "Particle-Imaging Techniques for Experimental Fluid Mechanics," Annual. Review Fluid Mech., 23, pp. 261-304.
- Buchave, P., 1992, "Particle Image Velocimetry-Status and Trends," Exp. Thermal and Fluid Sci., 5, pp. 586-604.
- Landreth, C.C., and Adrian, R.J., 1988, "Electrooptical Image shifting for particle image Velocimetry," Applied Optics, 27, pp. 4216-4220.
- Keane, R.D., and Adrian, R.J., 1990, "Optimization of Particle Image Velocimeters Part I: Double Pulsed Systems," Meas. Sci. Technol., 1, pp. 1202-1215.
- Paschal, K.B, Yao, C.S, and Ullrich S., 1994, "Spatial Resolution Effects on PIV Measurements in a Turbulent Wake Flow," AIAA 94-2297, 25th AIAA Fluid Dynamics Conference, June 20-23, 1994, Colorado Springs, CO.
- Hinze, J.O., 1987, Turbulence. McGraw-Hill, 2nd edition, Reissued 1987, pp. 546-558.
- Tennekes, H., and Lumley, J.L., 1972, A First Course in Turbulence. MIT Press, Cambridge, MA, pp. 49.

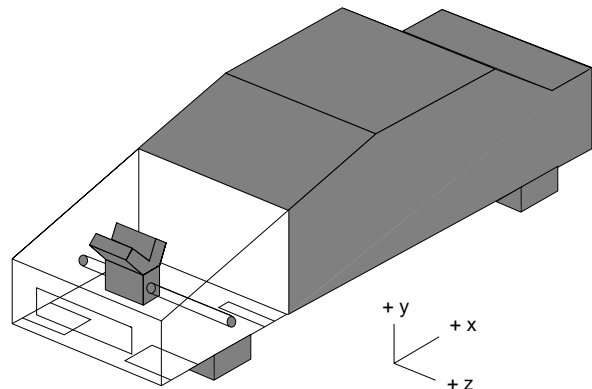


Figure 1. Boxcar schematic.

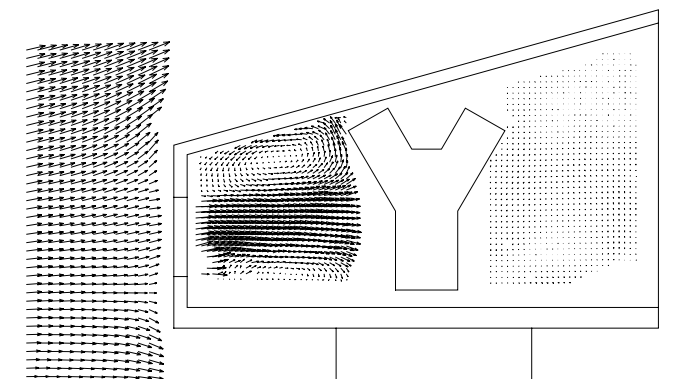
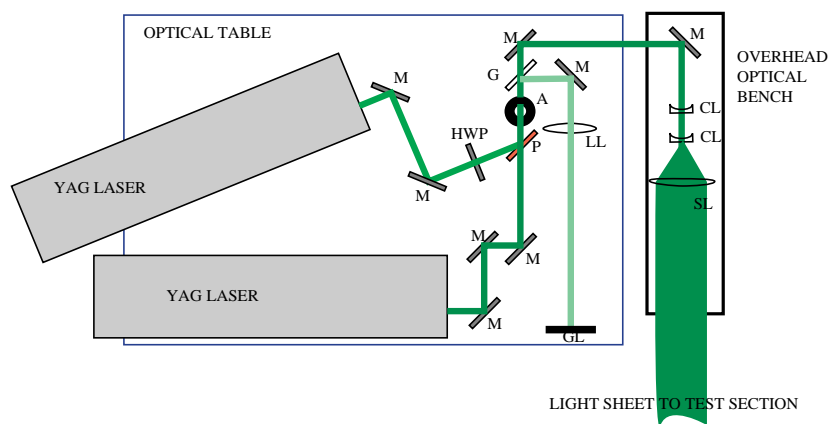


Figure 2. Boxcar mean flow field.



M: mirror
P: polarizer
A: aperture
G: glass
GL: ground glass
SL: spherical lens
LL: spherical lens
CL: cylindrical lens
CAL: calcite plate
HWP: half-wave plate

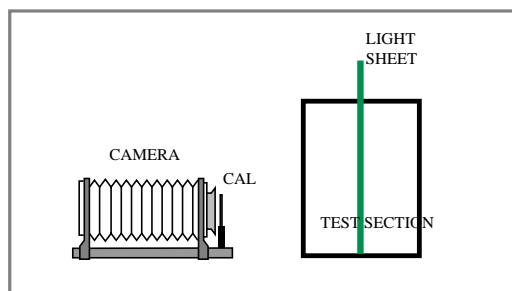


Figure 3. Laser and optics setup.

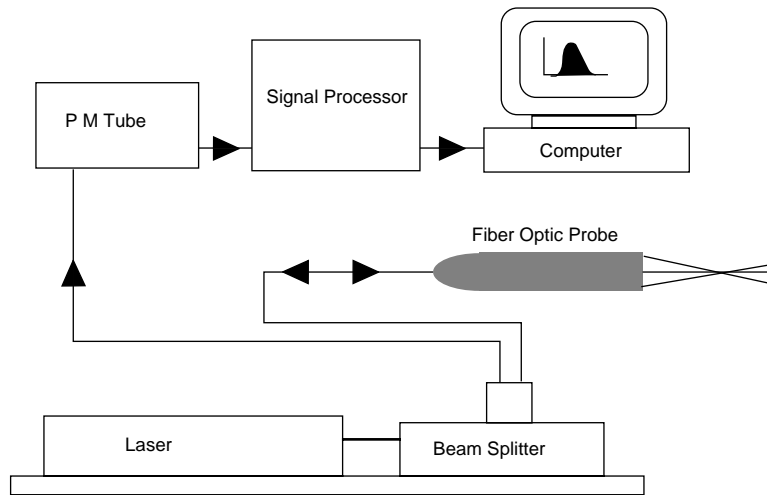


Figure 4. Schematic of LV system.

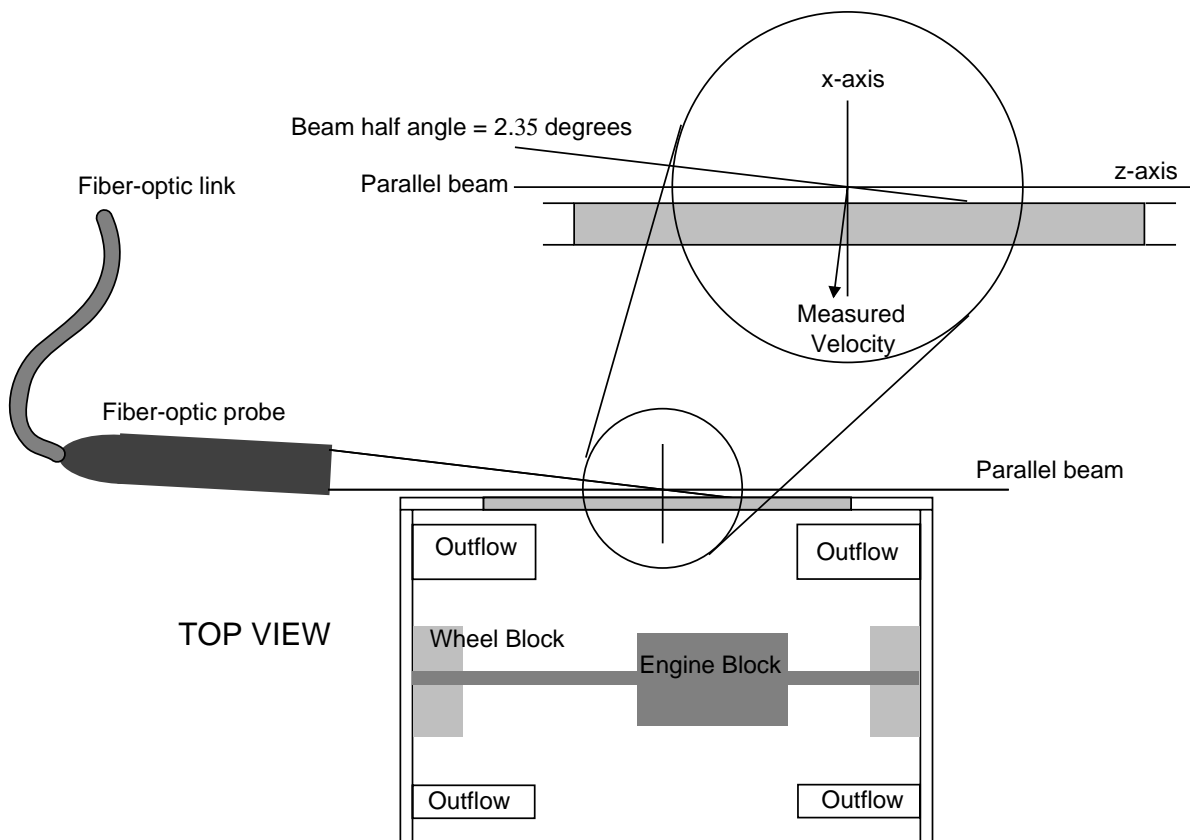


Figure 5. 1-D LV experimental setup.

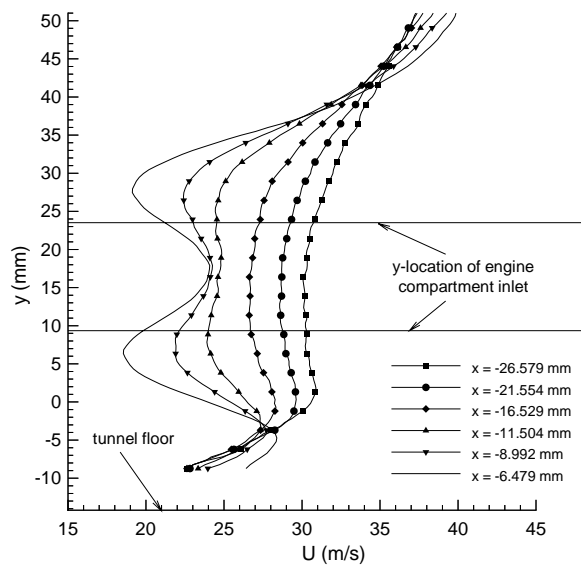


Figure 6. Freestream U profiles upstream of the Boxcar.

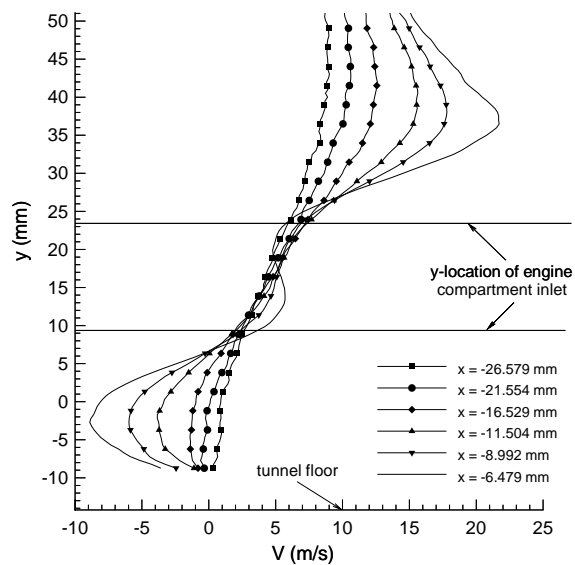


Figure 7. Freestream V profiles upstream of the Boxcar.

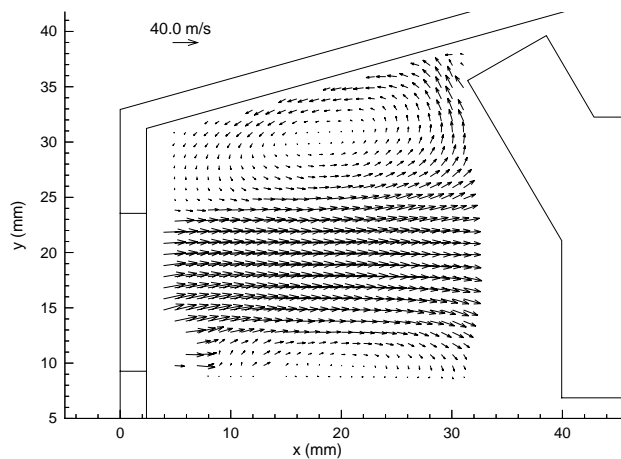


Figure 8. Underhood mean flow in front of the engine block.

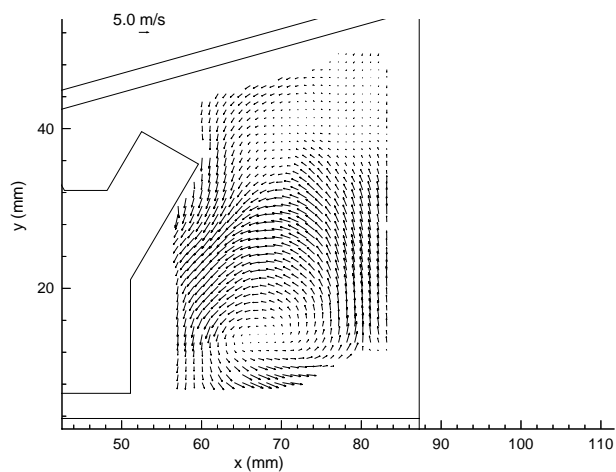


Figure 9. Underhood mean flow aft of the engine block.

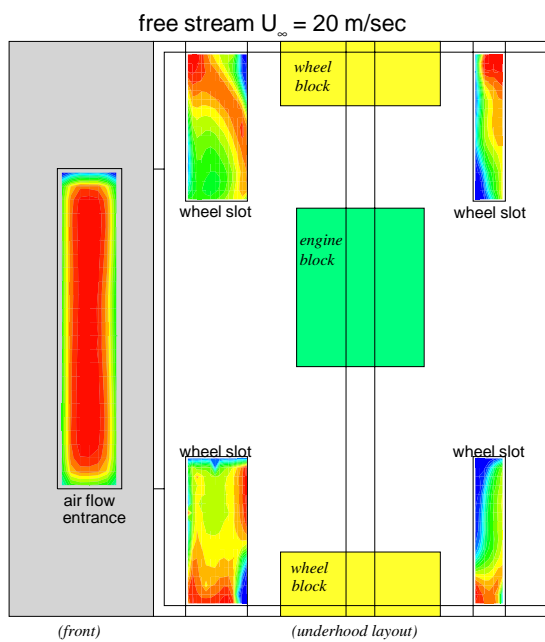


Figure 10. 1-D LV inflow and outflow patterns.

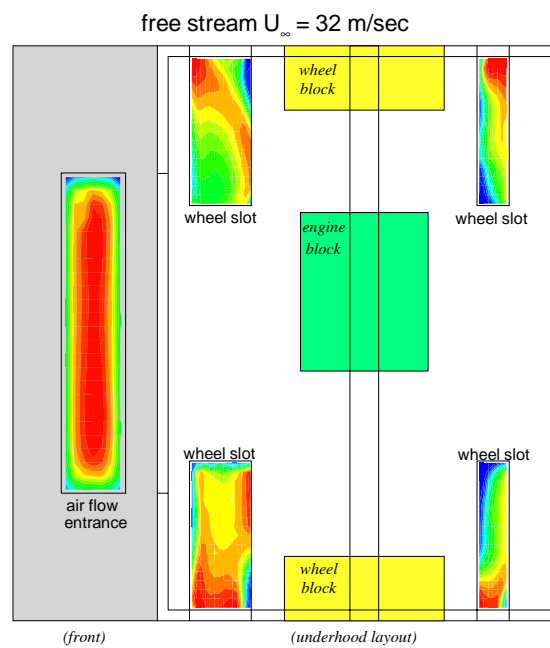


Figure 11. 1-D LV inflow and outflow patterns.

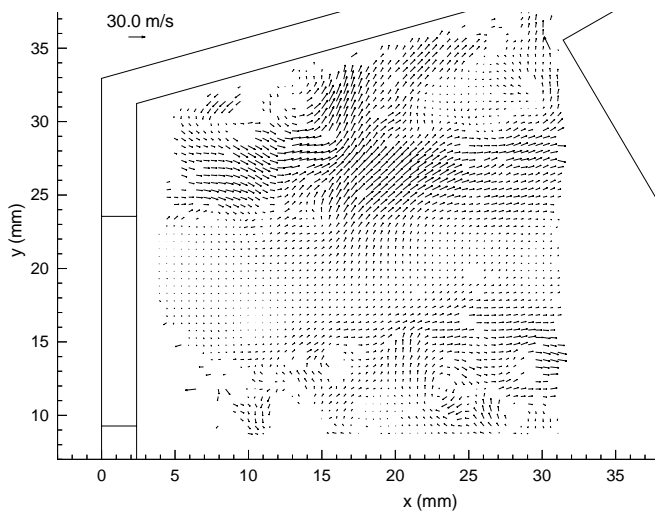


Figure 12. Fluctuating (u',v') field example 1.

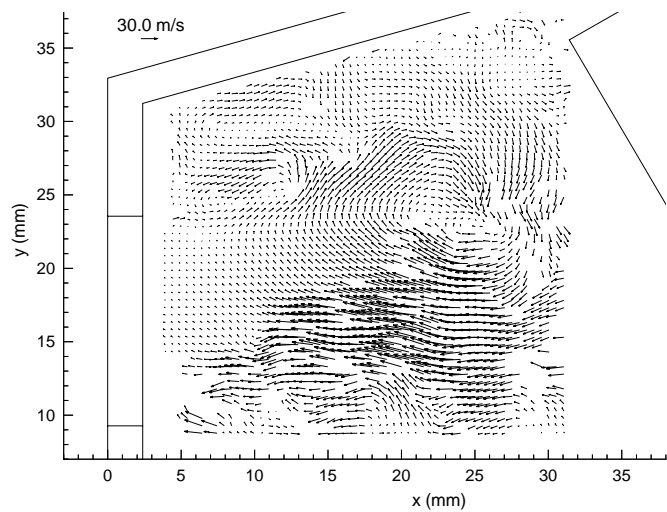


Figure 13. Fluctuating (u',v') field example 2.

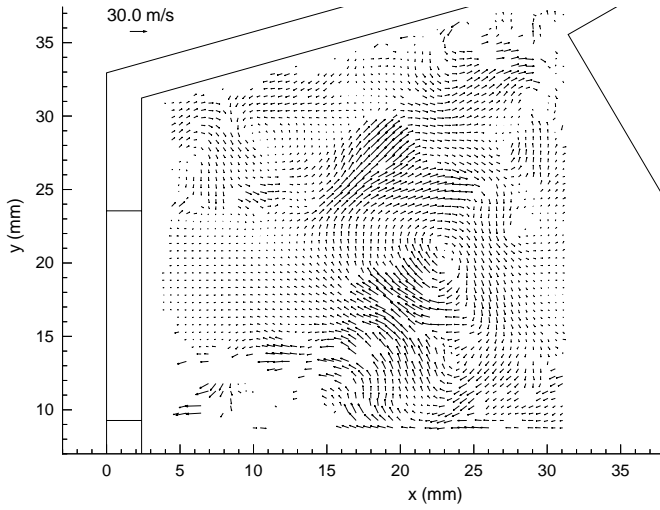


Figure 14. Fluctuating (u', v') field example 3.

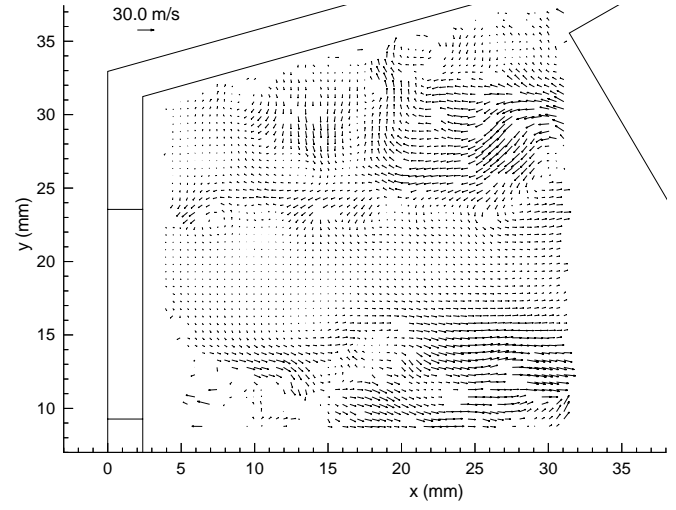


Figure 15. Fluctuating (u', v') field example 4.

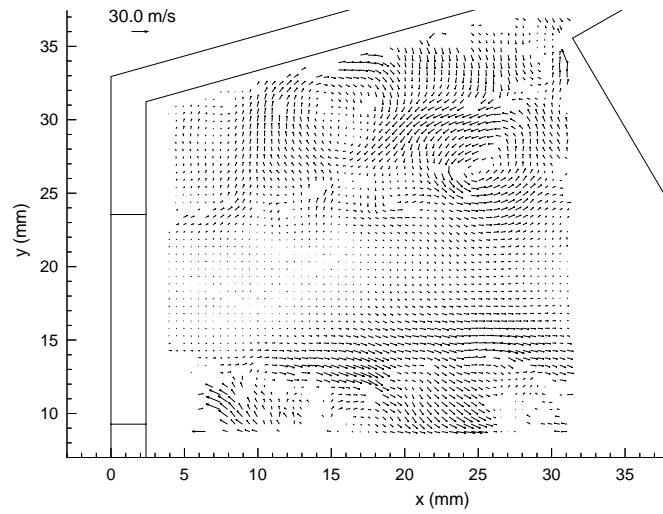


Figure 16. Fluctuating (u', v') field example 5.

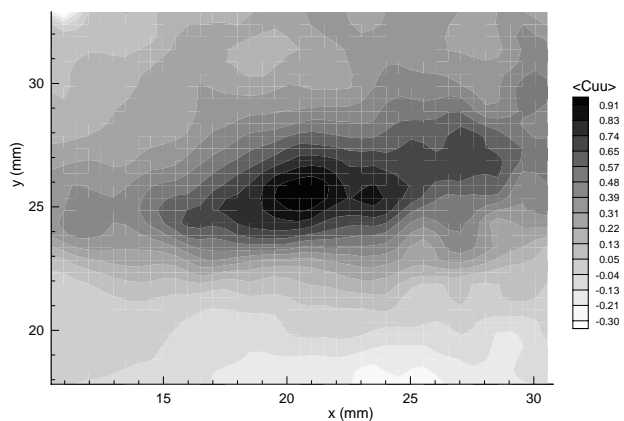


Figure 17. Two-point correlation $\langle C_{uu} \rangle$ $x, y = (20.5 \text{ mm}, 25.5 \text{ mm})$.

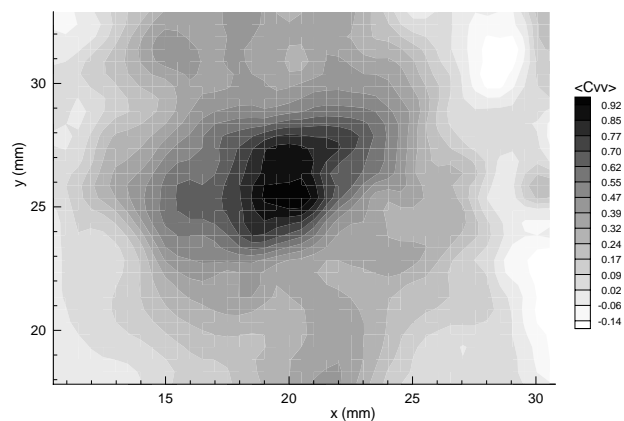


Figure 18. Two-point correlation $\langle C_{vv} \rangle$ $x, y = (20.5 \text{ mm}, 25.5 \text{ mm})$.

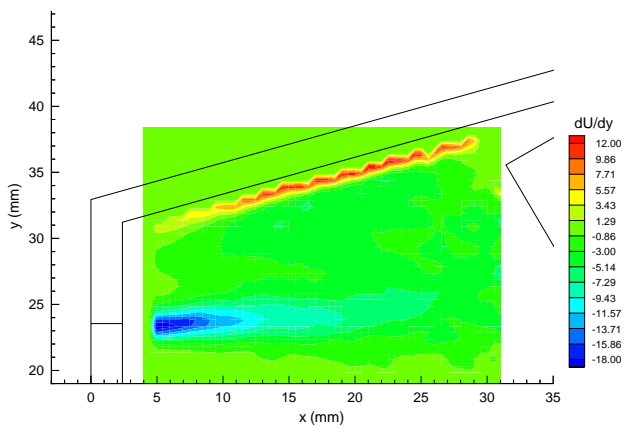


Figure 19. Velocity gradient contour plot.

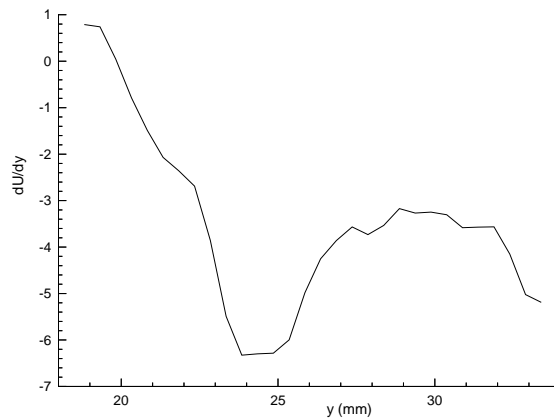


Figure 20. Velocity gradient profile, $x = 20.5 \text{ mm}$.

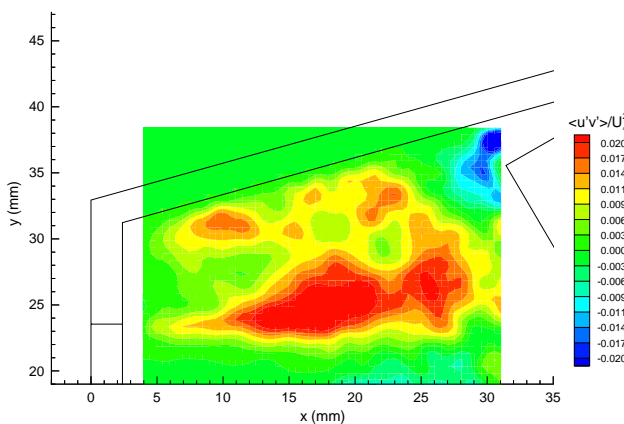


Figure 21. Upper shear Reynolds stress contour.

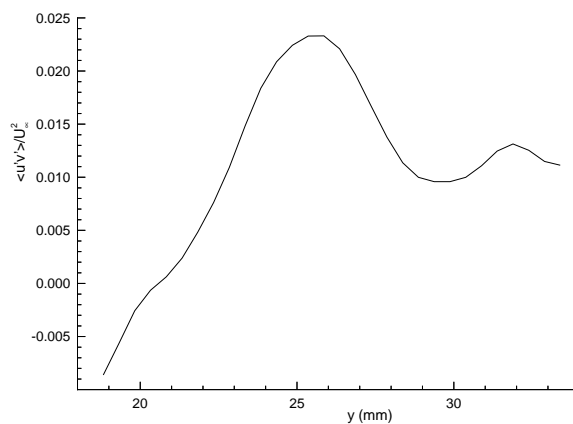


Figure 22. Reynolds stress profile, $x = 20.5 \text{ mm}$.

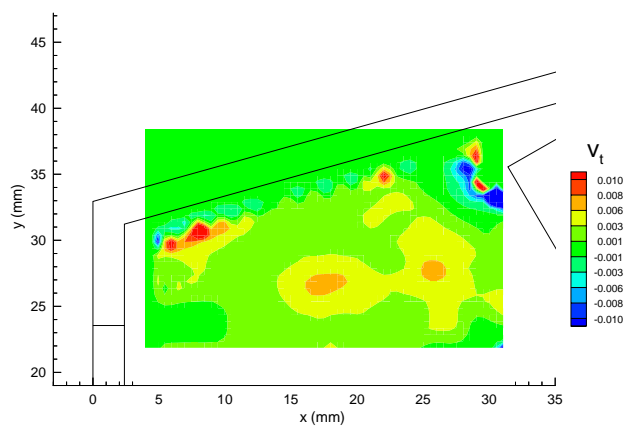


Figure 23. Upper shear eddy viscosity contour.

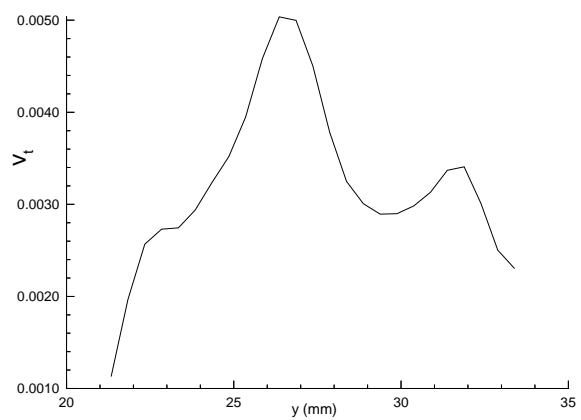


Figure 24. Upper shear eddy viscosity profile, $x=20.5$ mm.